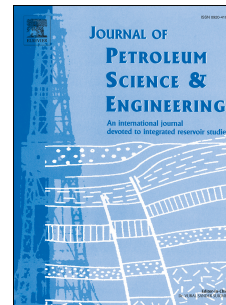


# Accepted Manuscript

A fracture conductivity model for channel fracturing and its implementation with Discrete Element Method

Haiyan Zhu, Jiadong Shen, Fengshou Zhang



PII: S0920-4105(18)30809-X

DOI: [10.1016/j.petrol.2018.09.054](https://doi.org/10.1016/j.petrol.2018.09.054)

Reference: PETROL 5317

To appear in: *Journal of Petroleum Science and Engineering*

Received Date: 9 May 2018

Revised Date: 6 September 2018

Accepted Date: 18 September 2018

Please cite this article as: Zhu, H., Shen, J., Zhang, F., A fracture conductivity model for channel fracturing and its implementation with Discrete Element Method, *Journal of Petroleum Science and Engineering* (2018), doi: <https://doi.org/10.1016/j.petrol.2018.09.054>.

This is a PDF file of an unedited manuscript that has been accepted for publication. As a service to our customers we are providing this early version of the manuscript. The manuscript will undergo copyediting, typesetting, and review of the resulting proof before it is published in its final form. Please note that during the production process errors may be discovered which could affect the content, and all legal disclaimers that apply to the journal pertain.

# A Fracture Conductivity Model for Channel Fracturing and Its Implementation with Discrete Element Method

Haiyan Zhu<sup>1,2</sup>, Jiadong Shen<sup>1</sup>, Fengshou Zhang<sup>3,4†</sup>

<sup>1</sup>State Key Laboratory of Oil and Gas Reservoir Geology and Exploitation, Southwest Petroleum University, Chengdu 610500, China

<sup>2</sup>State Key Laboratory of Nonlinear Mechanics (LNM), Institute of Mechanics, Chinese Academy of Sciences, Beijing 100190, China

<sup>3</sup>Department of Geotechnical Engineering, Tongji University, Shanghai 200092, China

<sup>4</sup>Key Laboratory of Geotechnical & Underground Engineering of Ministry of Education, Shanghai 200092, China

†E-mail of the corresponding author: [fengshou.zhang@tongji.edu.cn](mailto:fengshou.zhang@tongji.edu.cn)

**Abstract:** This paper introduces a new method to predict conductivity in channel fracturing by implementing analytical solution in Discrete Element Method (DEM). First, an analytical model for channel fracturing conductivity is proposed. Then, a DEM model calibrated by using experimental results is set up to investigate the deformation of proppant pillar. Finally, the analytical model of fracture conductivity is implemented in the DEM model to predict conductivity during fracture closing. Parametric analyses are carried out to understand the effects of four factors: proppant size combination, concentration, time ratio  $\tau$  and elastic modulus to stress ratio  $\lambda$ . Conductivity generally decreases during fracture closing and increases with the increasing proppant size and proppant concentration. The ratio of the pulsing time of proppant laden fluid to the pulsing time of the clean fluid is the key parameter for the field operation. A large time ratio could enhance the pillar stability though it may lead to the damage of fracture conductivity. For given rock modulus, closing stress and proppant size, the optimal range of time ratio can be given as a guidance for field operation. The field application of channel fracturing in the Shengli Oilfield proves that the optimized range of time ratio  $\tau$  based on the proposed theoretical model is valid. The porosity of proppant pillar first decreases due to compression and then increases during fracture closing period because of the breakdown of the proppant pillar and the resulted particle movement outward. This paper gives insights for understanding the channel fracture conductivity and provides a practical tool for the optimization of channel fracturing design in the field.

**Keywords:** channel fracturing; proppant pillar; fracture conductivity; optimization; Discrete Element Method

37 **List of Symbols**

38	$\tau$	The ratio of the pulsing time of proppant laden fluid to the pulsing time of
39		clean fluid, dimensionless
40	$\rho_s$	Pillar density, kg/mm <sup>3</sup>
41	$\rho_{pf}$	Density of proppant laden fluid, kg/mm <sup>3</sup>
42	$\mu$	Fluid dynamic viscosity, Pa·s
43	$\phi$	Pillar porosity, dimensionless
44	$\eta$	Effective perforation rate, dimensionless
45	$N$	Perforation number, dimensionless
46	$r$	Pillar radius, mm
47	$d_{ave}$	Average diameter of proppants, mm
48	$k_p$	Pillar permeability, mm <sup>2</sup>
49	$k_f$	Channel permeability, mm <sup>2</sup>
50	$k_i$	Permeability of area i, mm <sup>2</sup>
51	$k_0$	Fracture permeability in channel fracturing, mm <sup>2</sup>
52	$Q$	Flow rate of fracturing fluid, mm <sup>3</sup> /s
53	$Q_i$	Flow rate of area i, mm <sup>3</sup> /s
54	$t_p$	Pulsing time of proppant laden fluid, s
55	$t_f$	Pulsing time of clean fluid, s
56	$t_{tot}$	Duration of one pulsing period, s
57	$w_0$	Initial fracture aperture, mm
58	$w_f$	Fracture aperture, mm
59	$l$	Length of channel fracture, mm
60	$A_i$	Cross-section area of strip i, mm <sup>2</sup>
61	$\Delta p_p$	Pressure drop in pillar, Pa
62	$\Delta p$	Total pressure drop for strip i, Pa
63	$x$	Pillar length along x axis, mm
64	$\Delta y_i$	Width of strip i, mm
65	$E_c$	Apparent modulus in DEM, GPa
66	$k_n$	Contact normal stiffness in DEM, N/m
67	$k_s$	Contact shear stiffness in DEM, N/m
68	$\bar{k}^n$	Parallel bond normal stiffness in DEM, Pa/m
69	$\bar{k}^s$	Parallel bond shear stiffness in DEM, Pa/m
70	$D$	Particle diameter in DEM, mm
71	$K$	Conductivity, $\mu\text{m}^2\cdot\text{cm}$
72	$E$	Rock elastic modulus, GPa
73	$\sigma$	Closing stress, MPa
74	$\lambda$	The ratio of rock elastic modulus to closing stress, dimensionless

75

## 76 **1 Introduction**

77 In the past few years, channel fracturing has become an attractive completion technique  
78 in the oil and gas industry. Channel fracturing is firstly proposed by Gillard et al. (2010) and  
79 is mainly composed of three technical components, i.e., the pulse pumping technique, the  
80 multi-cluster perforating process, and the injection of fracturing fluid mixed with fibers.  
81 Fibers are added to proppant laden fluid to keep proppant pulses cohesive and prevent them  
82 from spreading when traveling through fracture slots. Proppant laden fluid and clean fluid are  
83 alternately injected into the rock formation with respectively specified amount of time to  
84 create proppant pillars. In the fracturing fluid flowback process, the void space between  
85 proppant pillars forms the highly conductive fluid channels which greatly improve the overall  
86 fracture conductivity during the production period.

87 The channel fracturing technique was first used to stimulate twelve full horizontal  
88 wellbores in the Eagle Ford formation in Hawkville field in October 2010. Production data  
89 indicated a 46% increase of condensate production (Rhein et al. 2011). Later applications of  
90 channel fracturing in Burgos basin, Talinskoe oilfield, Egyptian western desert, Taylakovskoe  
91 oil field, Ordos Basin, South East Kuwait, Barnett Shale, further confirmed the feasibility of  
92 this technique which managed to save 43% of proppant usage by average (Valenzuela et al.  
93 2012; Kayumov et al. 2012; Gawad et al. 2013; Valiullin et al. 2015; Li et al. 2015; Gazi et al.  
94 2016; Samuelson et al. 2012; Medvedev et al. 2013). Application of channel fracturing in  
95 tight oil and gas reservoirs in Ordos Basin, China produced 2.4 times as much oil and 4 to 5  
96 times as much gas as conventional fracturing did (Li et al. 2015).

97 Discrete pillars created by channel fracturing set a totally different transportation pattern  
98 for proppants and hydrocarbons from conventional fracturing, to which conventional  
99 theoretical models to study proppant embedment and conductivity are no longer applicable. In  
100 recent years, a number of studies were carried out to investigate the mechanism of channel  
101 fracturing. Gillard et al. presented a laboratory study on channel fracturing conductivity and  
102 the results showed that the permeability of channel fracturing fractures was 1.5 to 2.5 orders  
103 higher than that of conventional fracturing fractures (Gillard et al. 2010). Nguyen et al.  
104 conducted a series of experiments to study the stability of proppant pillars (2014). A fast  
105 compression stage could be observed in stress-strain curves of proppant pillars. Zhang et al.  
106 studied proppant embedment and conductivity by using surface modification agent (SMA)  
107 treated proppants for both traditional and channel fracturing (Zhang 2014; Zhang and Hou  
108 2016). Yan et al. developed an analytical model to represent the physical deformation of  
109 channel-fracturing fractures and Darcy-Brinkman equation was applied to simulate flow in  
110 pillars and fluid channels (Yan et al. 2016). Zheng et al. derived the formula of fracture  
111 conductivity based on Hertz contact theory and analyzed the effects of proppant distribution  
112 density and proppant pillar radius on fracture conductivity (Zheng et al. 2017). Hou et al. used  
113 Kelvin-Voigt model to describe the viscoelastic deformation of proppants and rock based on

114 theoretical models proposed by Li et al. (Hou et al. 2016; Li et al. 2015). Guo et al.  
115 established an analytical model to describe fracture aperture change and conductivity for  
116 cuboid shaped pillars (Guo et al. 2017). Most of the above studies were conducted on the  
117 basis of classical Hertz contact theory. But few of them paid attention to fracture deformation  
118 when calculating the fracture aperture. More importantly, proppant pillars were hypothetically  
119 deemed as a continuum by using Hertz contact theory. The microstructure, as well as the  
120 mechanical properties of proppant pillar may change dramatically under increasing loadings  
121 with the given nature of porous media. As one of the key factors in investigating channel  
122 fracturing conductivity, the constitutive behavior of proppant pillars is not properly realized in  
123 these studies.

124 Hou et al. assumed that proppant pillars were standard cylindrical indenters based on  
125 Hertz contact theory (Hou et al. 2016). Pillar spacing and pulsing time were used to optimize  
126 the residual fracture aperture. Meyer et al. presented a solution methodology for designing  
127 open channels and for flow around pillars in propped fractures (Meyer et al. 2014).  
128 Conductivity were formulated for different types of channel based on analysis of half-space  
129 loading property. These two solutions took fracture deformation into consideration, which  
130 was ignored in studies mentioned before. But proppant pillars were assumed to be rigid body.  
131 This assumption, contradictory with the physical reality, may result in inaccuracy when pillar  
132 deformation plays a major role during fracture closing.

133 Discrete Element Method (DEM) was first proposed by Cundall and Strack to study the  
134 mechanical characteristics of rock and soils (Cundall and Strack 1979). In Recent years, it has  
135 been widely used to study the mechanism of hydraulic fracturing (Zhou et al 2015a, Zhou et  
136 al 2015b b, Zhang et al. 2017), however, the application of DEM on proppant conductivity is  
137 less often seen. The first DEM study of proppant stability can be traced back to 1995. Asgian  
138 et al. first used DEM to study the mechanism of proppant backproduction in hydraulic  
139 fracturing (Asgian et al. 1995). Later, Deng et al. proposed a DEM model to investigate the  
140 shale–proppant interactions and evaluate the fracture aperture under different proppant sizes,  
141 Young's moduli and pressure levels (Deng et al. 2014). Zhang et al. developed an integrated  
142 DEM-CFD modeling work flow to model proppant embedment and fracture conductivity  
143 (Zhang et al. 2017). Bolintineanu et al. studied the effects of proppant packings on porosity,  
144 permeability and conductivity by using DEM (Bolintineanu et al. 2017). Zhu et al. (2018)  
145 simulated the deformation and stability properties of proppant pillar during flowback with  
146 DEM-CFD coupling method. The effects of fibers are modeled by implementing the bonded  
147 particle model. Several phenomena are observed with relation to flow and proppant pillar  
148 distribution, which promotes current understandings for channel fracturing.

149 Various analytical models have been proposed to predict the change of fracture opening  
150 and conductivity for channel fracturing. But few of them investigated the constitutive  
151 characteristics of proppant pillar. Pillar deformation was calculated by taking a pillar as an  
152 entity instead of an assembly of particles. In this study, we firstly propose an analytical model

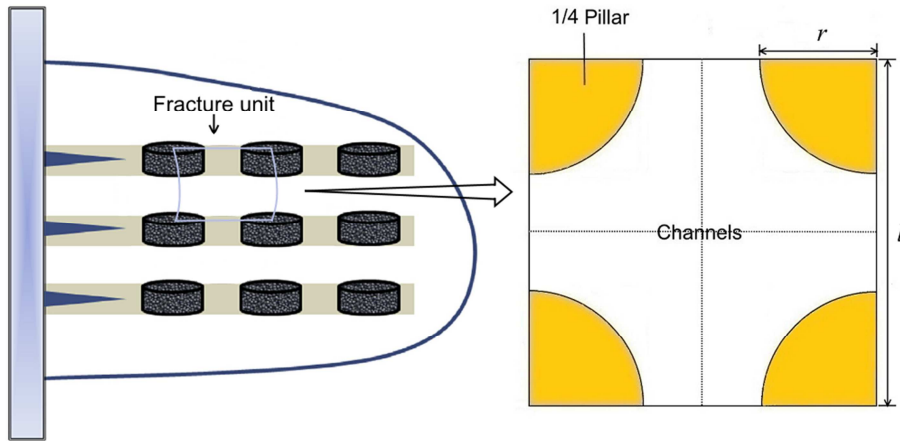
153 for channel fracturing conductivity. The analytical solution is then implemented in DEM  
 154 modeling. The DEM model can calculate the fracture conductivity while considering the  
 155 pillar deformation at different closing stress. The effects of proppant size combination,  
 156 proppant concentration, the ratio of the pulsing time of proppant laden fluid to the pulsing  
 157 time of the clean fluid, and the ratio of rock modulus to closing stress are investigated.

## 158 2 An analytical model of channel fracturing conductivity

159 Figure 1 plots the schematic of pillars and fluid channels of channel fracturing. The  
 160 yellow quarter disks represent the proppant pillars and the rest of the area in the plot  
 161 represents the fluid channels, assuming that proppant pillars are arranged in the matrix form  
 162 with uniform spacing. The pumping schedule of channel fracturing alternates the proppant  
 163 laden fluid pulse and the clean fluid pulse. According to Zheng et al. (2017), for a proppant  
 164 laden fluid pulse, the following equation can be derived,

$$165 \quad \pi r^2 w_0 \rho_s = \frac{t_p Q \rho_{pf}}{N \eta} \quad (1)$$

166 where  $r$  is pillar radius, mm;  $w_0$  is initial fracture aperture, mm;  $\rho_s$  is pillar density, kg/mm<sup>3</sup>;  
 167  $t_p$  is the pulsing time of proppant laden fluid, s;  $Q$  is flow rate (constant in both proppant laden  
 168 stages and clean fluid stages), mm<sup>3</sup>/s;  $\rho_{pf}$  is the density of proppant laden fluid, kg/mm<sup>3</sup>;  
 169  $N$  is perforation number, dimensionless;  $\eta$  is the effective perforation rate, dimensionless.



170  
 171 **Figure 1** Schematic of pillars and fluid channels of channel fracturing  
 172

173 Considering that the proppant laden fluid is incompressible, it's reasonable to assume  
 174 that pillar density  $\rho_s$  is equal to the density of proppant laden fluid  $\rho_{pf}$ . Eq. (1) is then rewritten  
 175 as,

$$176 \quad \pi r^2 w_0 = \frac{t_p Q}{N \eta} \quad (2)$$

177 A similar relationship can be found in one pulsing period,

$$178 \quad l^2 w_0 = \frac{t_{\text{tot}} Q}{N \eta} \quad (3)$$

$$179 \quad t_{\text{tot}} = t_p + t_f \quad (4)$$

180 where  $l$  is the length of a channel fracture in Figure 1, mm;  $t_{\text{tot}}$  is the duration of one pulsing  
 181 period, s;  $t_f$  is the pulsing time of clean fluid, s.

182 Combining Eqs. (2) – (4), in one pulsing period, the ratio of the pulsing time of proppant  
 183 laden fluid to the pulsing time of the clean fluid is expressed as,

$$184 \quad \tau = \frac{t_p}{t_f} = \frac{\pi (r/l)^2}{1 - \pi (r/l)^2} \quad (5)$$

185 where  $r/l$  lies in the range of [0, 0.5].

186  $r/l$  is an index for the stability of proppant pillars. If  $r/l$  is too small, the fracture might  
 187 not be effectively propped and the fracture conductivity cannot be sustained. On the other  
 188 hand, if  $r/l$  is too larger, the fracture is effectively propped by pillars, but the fracture  
 189 conductivity can be limited due to narrow fluid channels. An optimized time ratio  $\tau$  then can  
 190 be obtained, which meets the requirement of proppant stability but also gives the maximum  
 191 fracture conductivity.

192 The permeability of proppant pillar and fluid channel can be calculated separately. The  
 193 permeability of proppant pillar  $k_p$  is calculated based on Kozeny-Carman formula in Eq. (6)  
 194 and the permeability of fluid channel  $k_f$  is calculated using the parallel plate model in Eq. (7)  
 195 (Gillard et al. 2010; Bear 1972). Both pillar porosity  $\phi$  and fracture aperture  $w_f$  in Eq. (6) and  
 196 Eq. (7) need to be obtained from numerical simulation.

$$197 \quad k_p = \frac{d_{\text{ave}}^2 \phi^3}{180(1-\phi)^2} \quad (6)$$

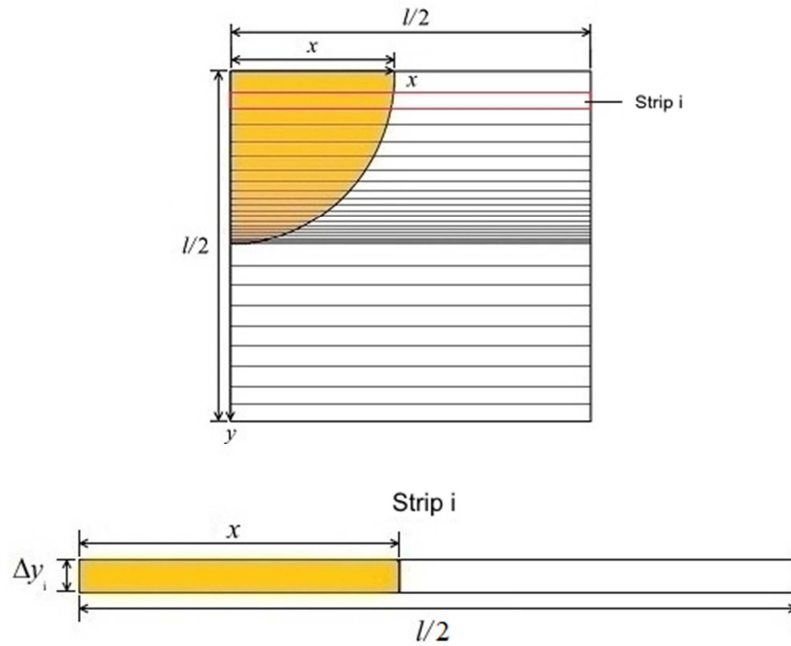
$$198 \quad k_f = \frac{w_f^2}{12} \quad (7)$$

199 where  $k_p$  is proppant pillar permeability,  $\text{mm}^2$ ;  $k_f$  is fluid channel permeability,  $\text{mm}^2$ ;  $d_{\text{ave}}$  is the  
 200 average diameter of proppants, mm;  $\phi$  is pillar porosity, dimensionless;  $w_f$  is fracture aperture,  
 201 mm.

202 The schematic plot in Figure 1 can be further divided into four equal pieces. We further  
 203 take one piece as a calculation unit. As shown in Figure 2, the seepage area is cut into small  
 204 strips. Zheng et al. (2017) derived fracture permeability by ignoring the pressure drop of fluid  
 205 channel in strips. Here we consider the pressure drop for both proppant pillars and fluid  
 206 channels. Applying Darcy's law to the strip  $i$  in Figure 2, we can get the following  
 207 relationship,

$$208 \quad Q_i = \frac{k_p A_i \Delta P_p}{\mu x} = \frac{k_f A_i (\Delta P - \Delta P_p)}{\mu (l/2 - x)} = \frac{k_i A_i \Delta P}{\mu l/2} \quad (8)$$

209 where  $Q_i$  is the flow rate of strip  $i$ ,  $\text{mm}^3/\text{s}$ ;  $k_i$  is fracture permeability,  $\text{mm}^2$ ;  $A_i$  is the  
 210 cross-section area,  $\text{mm}^2$ ;  $\mu$  is fluid dynamic viscosity,  $\text{Pa}\cdot\text{s}$ ;  $\Delta p_p$  is pressure drop in pillar,  $\text{Pa}$ ;  
 211  $\Delta p$  is the total pressure drop for strip  $i$ ,  $\text{Pa}$ ;  $x$  is pillar length along  $x$  axis,  $\text{mm}$ ;  $l/2$  is the length  
 212 of strip  $i$  and half fracture length in Figure 1,  $\text{mm}$ .



213  
 214 **Figure 2** Partition of one calculation unit into several seepage strips

215  
 216 The permeability of strip  $i$  is rewritten as,

$$217 \quad k_i = \frac{k_p k_f l}{k_p l + 2(k_f - k_p)x} \quad (9)$$

218 Thus the permeability of channel fracture is expressed by using integration,

$$219 \quad k_0 = \sum_{i=1}^n k_i \frac{\Delta y_i}{l/2} = \int_0^l \frac{2k_p k_f}{k_p l + 2(k_f - k_p)x} dy \quad (10)$$

220 where  $\Delta y_i$  is the width of strip  $i$ ,  $\text{mm}$ ;  $k_0$  is channel fracture permeability,  $\text{mm}^2$ .

221 When  $y > r$ ,  $x=0$ . Therefore, the fracture permeability is rewritten as

$$\begin{aligned}
 k_0 &= \int_0^r \frac{2k_p k_f}{k_p l + 2(k_f - k_p)x} dy + \int_r^{\frac{l}{2}} \frac{2k_f}{l} dy \\
 &= \int_0^r \frac{2k_p k_f x}{[k_p l + 2(k_f - k_p)x](r^2 - x^2)^{0.5}} dx + k_f \left(1 - \frac{2r}{l}\right)
 \end{aligned}
 \tag{11}$$

222

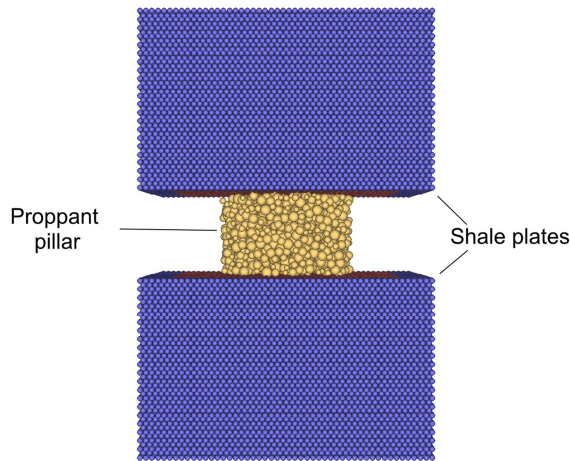
223 Accordingly, the channel fracture permeability  $k_0$  can be calculated from Eq. (11), where  
 224  $k_p$  and  $k_f$  are determined from Eq. (6) and Eq. (7), respectively.

### 225 3. Implementation of channel fracturing conductivity model with DEM

#### 226 3.1 DEM model setup

227 DEM models the movement and interaction of particles in granular material. Physical  
 228 properties of particles are predetermined by assigning micro-parameters like stiffness and  
 229 bond strength for particles and contact nodes between them. These micro-parameters can be  
 230 then adjusted to reproduce the macroscopic properties of granular material (Cundall and  
 231 Starfield 1979, Potyondy and Cundall 2004).

232 Figure 3 shows the numerical model for studying channel fracturing based on DEM. The  
 233 upper and lower shale plates are composed of blue particles arranged in a body-centered  
 234 structure, while the proppant pillar is composed of particle assembly in yellow. Two plates are  
 235 loaded with up to 50 MPa stress to model fracture closing and pillar deformation.



236

237

**Figure 3** DEM model for channel fracturing

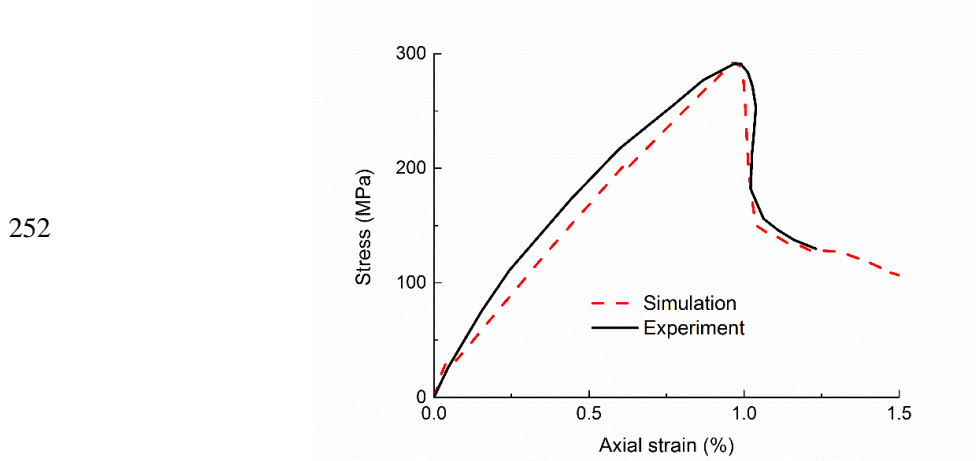
238

#### 239 (1) Rock property calibration

240 The model is benchmarked by comparing the experimental results and DEM modeling  
 241 results of triaxial tests, as shown in Figure 4. Rock cores from Shengli oilfield, China are  
 242 processed into 9 samples with diameter of 25 mm and height of 50 mm. Triaxial tests are  
 243 carried out on 9 rock core samples using RTR-1000 triaxial testing system. Results show rock

244 elastic modulus of 28.6-40.9GPa, Poisson's ratio of 0.25-0.28 and compressive strength of  
245 200.7-230.2 MPa.

246 Table 1 lists the micro-scale parameters used in numerical triaxial tests. The bonded  
247 particle model (Potyondy and Cundall 2004) is implemented to simulate the rock material.  
248 Since the modulus and strengths of rock can be independent of the particle size in DEM, rock  
249 particles are generated in same radius of 0.2 mm to achieve effective computation (Ma and  
250 Huang 2018a). The same micro-scale parameters are used in the following sections for  
251 numerical investigations.



253 **Figure 4** Stress-strain curves of X23 sample from laboratory triaxial test and DEM triaxial test

254

255

**Table 1** Micro-scale parameters of rock

Linear contact	Apparent modulus	5.7
	$E_c$ /GPa	
	Normal stiffness	$2.6k_s$
	$k_n$ /(N/m)	
	Shear stiffness $k_s$ /(N/m)	$2DE_c$
Micro-parameters	Apparent modulus	5.7
	$E_c$ /GPa	
	Normal stiffness $\bar{k}^n$	$2.6\bar{k}^s$
	/(Pa/m)	
	Shear stiffness $\bar{k}^s$	$E_c/D$
	/(Pa/m)	
	Parallel bonds	
Normal bond strength/MPa	38	
Shear bond strength	38	
/MPa		
Radius multiplier	1	
Friction	0.5	
Density/(kg/m <sup>3</sup> )	2650	

256

257 **(2) Proppant pillar property calibration**

258       Fibers used in proppant-laden fluid increase the inter-particle cohesion and friction,  
 259       which can enhance the stability of proppant pillars and resist the fracture closing. In order to  
 260       include this effect, proppant particles are allowed to bond with each other, similar with the  
 261       rock material. The microscale parameters for proppant particles in the DEM model are  
 262       calibrated by comparing the experimental results and DEM modeling results of proppant  
 263       pillar compression. Figure 5 shows proppant pillar in experiment, made up with Combo  
 264       proppants and short fibers, and proppant pillar in DEM modeling. Table 2 lists the microscale  
 265       parameters for proppant particles after the calibration (see Figure 6).

266       It should be noted that, in Figure 6, the initial quick drop of the curves in the experiments  
 267       might be related to the initial loose packing state, while the numerical curves appear to be  
 268       smoother. Though results from simulation are different from experimental results when the  
 269       closing stress is less than 10 MPa, it shows good agreement with experimental results under  
 270       high stresses. Since the real underground stress is rather high, the stress-strain relationship of  
 271       proppant pillar under high stresses, which is well calibrated, is the key factor that determines  
 272       the effectiveness of calibration.



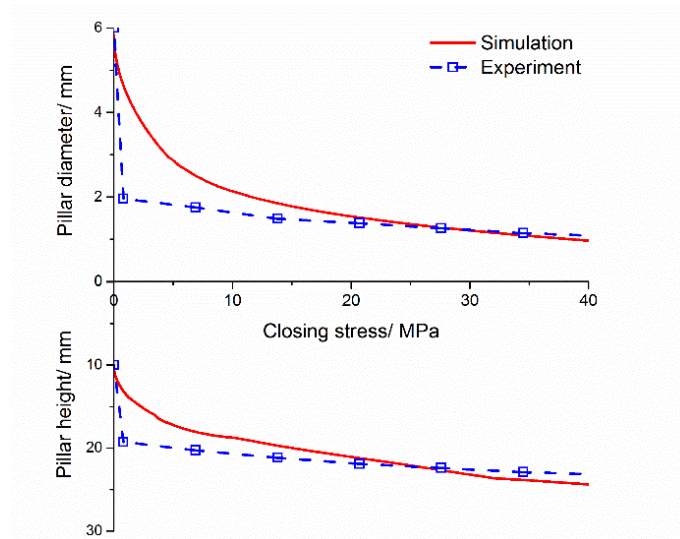
273  
 274       **Figure 5** (a) proppant pillar in experiment, (b) proppant pillar in DEM modeling

275  
 276       **Table 2** Micro-scale parameters of proppants

	Size combination	40/70	30/50	20/40	
Micro-parameters	Linear contact	Apparent modulus		85	
		$E_c/\text{MPa}$			
		Normal stiffness		$2DE_c$	
		$k_n/(\text{N/m})$			
		Shear stiffness $k_s/(\text{N/m})$		$k_n$	
	Parallel bonds	Apparent modulus		85	
		$E_c/\text{MPa}$			
		Normal stiffness $\bar{k}^n$			$E_c/D$
		$/(\text{Pa/m})$			
		Shear stiffness $\bar{k}^s$			$\bar{k}^n$
	$/(\text{Pa/m})$				
	Normal bond strength		500		

	/MPa			
Shear bond strength				500
	/MPa			
Radius multiplier				1
Friction				0.9
Density /(kg/m <sup>3</sup> )				2650
Particle radius (D/2)/mm	0.21-0.42	0.3-0.6	0.42-0.84	

277



278

279 **Figure 6** Comparison between numerical and experimental testing results for pillar compression

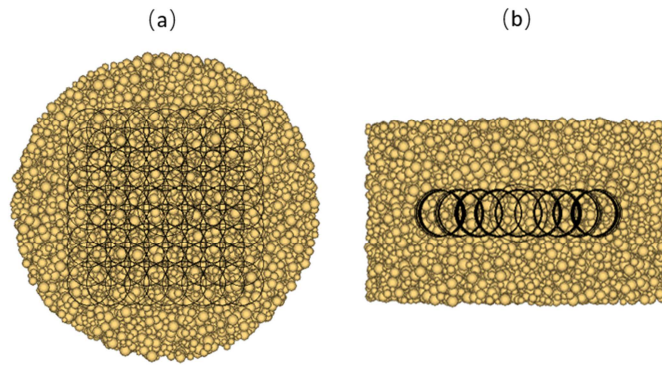
280

### 281 3.2 Acquisition of porosity and fracture aperture

282 While fracture permeability can be calculated from Eq. (11), pillar porosity and fracture  
 283 aperture need to be obtained from DEM simulation in advance.

#### 284 (1) Acquisition of proppant pillar porosity

285 During the fracture closing process, proppant pillar porosity changes with increasing  
 286 stress. The “measurement sphere” logic is applied to log the pillar porosity. The measurement  
 287 sphere needs to be larger enough to be a representative element volume but also small enough  
 288 to maintain the accuracy. Meanwhile, the size of the measurement sphere should also be  
 289 smaller than the aperture after the closing so that no particle from the rock plate is included in  
 290 the measurement sphere. Thus, the size of the measurement sphere is set to be 7 times particle  
 291 size. Figure 7 shows a total of 81 small measurement spheres in the proppant pillar for  
 292 logging pillar porosity in this DEM investigation.

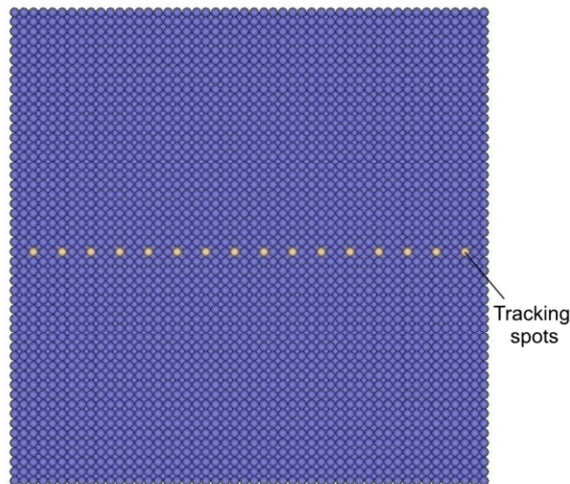


293  
294 **Figure 7** Placement of 81 small measurement spheres in the pillar, (a) top view, and (b) lateral view

295

## 296 (2) Acquisition of fracture aperture

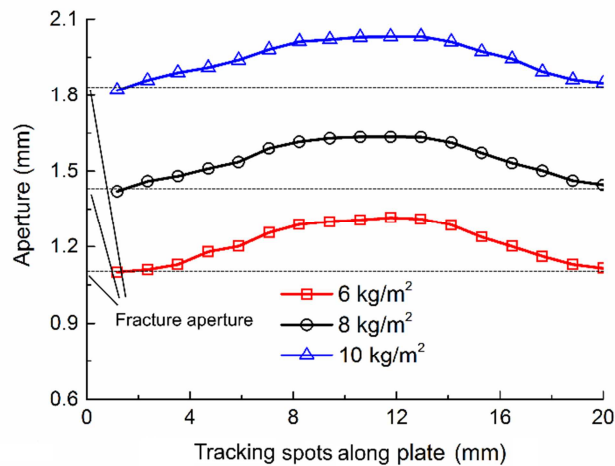
297 Figure 8 shows some particles on the fracture walls that are used tracking spots for  
298 logging the fracture aperture width. Figure 9 shows aperture distribution along the fracture  
299 wall at the closing stress of 41.4 MPa for three proppant concentrations. As expected,  
300 apertures near the center of plate (where fracture is supported by the proppant pillar) tend to  
301 be larger than those at the far ends of plate (where flow channel lies). In this study, we chose  
302 the fracture apertures measured at the far ends of plate for any calculation.



303

304 **Figure 8** Particles for logging fracture apertures along fracture wall

305



306  
307 **Figure 9** Aperture distribution along the fracture wall (under 41.4 MPa stress)  
308

### 309 3.3 Calculation of fracture conductivity

310 After gaining the porosity and fracture aperture from DEM simulation, Eq. (6) and Eq. (7)  
311 are solved to get pillar permeability  $k_p$  and channel permeability  $k_f$  and therefore channel  
312 fracture permeability  $k_0$  can be calculated by using Eq. (11). Finally, the fracture conductivity  
313 is calculated as follows,

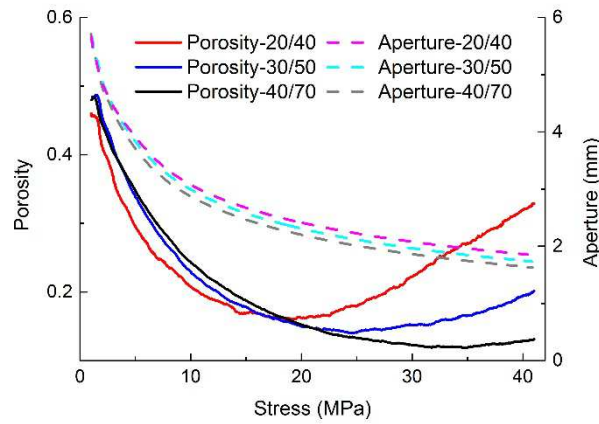
$$314 \quad K = k_0 w_f \quad (12)$$

315 where  $K$  is fracture conductivity,  $\mu\text{m}^2 \cdot \text{cm}$ .

## 316 4 Parametric analysis of channel fracture conductivity

### 317 4.1 Effect of proppant size combination

318 Figure 10 shows the proppant pillar porosity and fracture aperture at different closing  
319 stress for three proppant size combinations, 20/40 mesh, 30/50 mesh and 40/70 mesh. The  
320 proppant concentration is  $8 \text{ kg/m}^3$  for all three cases. The height and diameter of the proppant  
321 pillar are 6 mm and 10 mm, respectively. The elastic modulus of the reservoir rock is 32 GPa.  
322 The same proppant pillar size and reservoir rock elastic modulus are applied to all cases in  
323 this study unless specifically mentioned. It can be seen that all three cases have the same U  
324 shape curves indicating that the proppant pillar porosity decreases first and then increases  
325 with the closing stress. The 20/40 mesh case has the most reversing trend of porosity change  
326 while the 40/70 mesh has the least. As the closing stress increases, the fracture aperture  
327 gradually decreases. Smaller proppant size has larger aperture decrease during closing,  
328 consistent with the results of uniform layer of proppant (Zhang et al. 2017).

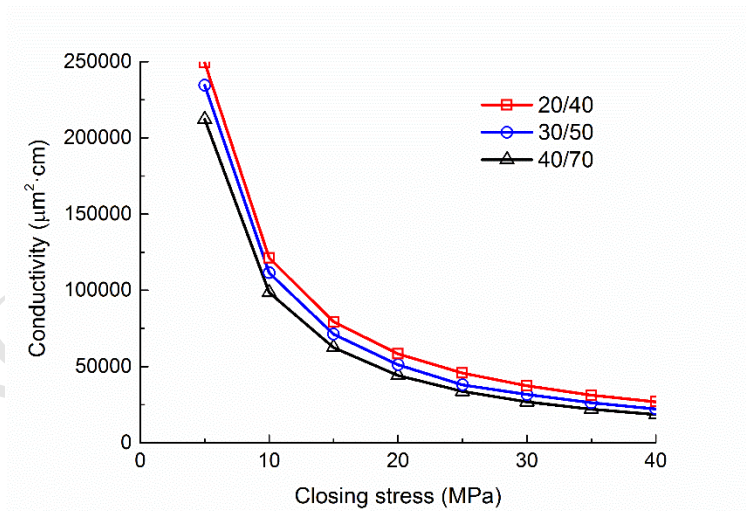


329

330 **Figure 10** Proppant pillar porosity and fracture aperture at different closing stress for three proppant  
 331 size combinations, 20/40 mesh, 30/50 mesh and 40/70 mesh

332

333 Figure 11 shows the fracture conductivity, calculated based on Eq. (12), at different  
 334 closing stress for three proppant size combinations. The 20/40 mesh case has the largest  
 335 aperture after closing, therefore it has the largest  $k_f$  based on Eq. (7). Meanwhile, although  
 336 Figure 10 shows that the proppant pillar porosity with 20/40 mesh is slightly smaller than the  
 337 other two cases at closing stress below 18 MPa, with the advantage of larger particle size, it  
 338 still keeps the largest  $k_p$  based on Eq. (6). Thus, similar to the conventional fracturing method  
 339 with uniform layer of proppant, large proppant size leads to better fracture conductivity after  
 340 closing.



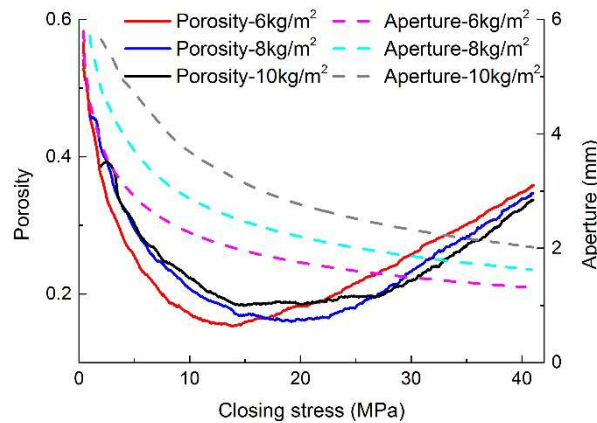
341

342 **Figure 11** Fracture conductivity at different closing stress for three proppant size combinations, 20/40  
 343 mesh, 30/50 mesh and 40/70 mesh

344

## 345 4.2 Effect of proppant concentration

346 Figure 12 shows the proppant pillar porosity and fracture aperture at different closing  
 347 stress for three proppant concentrations,  $6 \text{ kg/m}^3$ ,  $8 \text{ kg/m}^3$ , and  $10 \text{ kg/m}^3$ . All three cases have  
 348 the same proppant size of 20/40 mesh. With the same size of proppant pillar, the case with 6  
 349  $\text{kg/m}^3$  has the loosest initial proppant pack and the case with  $10 \text{ kg/m}^3$  has the densest initial  
 350 proppant pack. The proppant pillar porosity for all three cases has the similar decreasing to  
 351 increasing transition as the closing stress gradually increases. The fracture for these three  
 352 cases decreases rapidly initially and levels off as the closing stress increases. The aperture  
 353 difference among these three cases increases first due to the varied compaction and decreases  
 354 towards the end of the loading. The aperture difference between  $10 \text{ kg/m}^3$  and  $8 \text{ kg/m}^3$  is 0.82  
 355 mm with the closing stress of 10 MPa, and reduces to 0.39 mm at the end of the loading with  
 356 the closing pressure of 41.4 MPa.

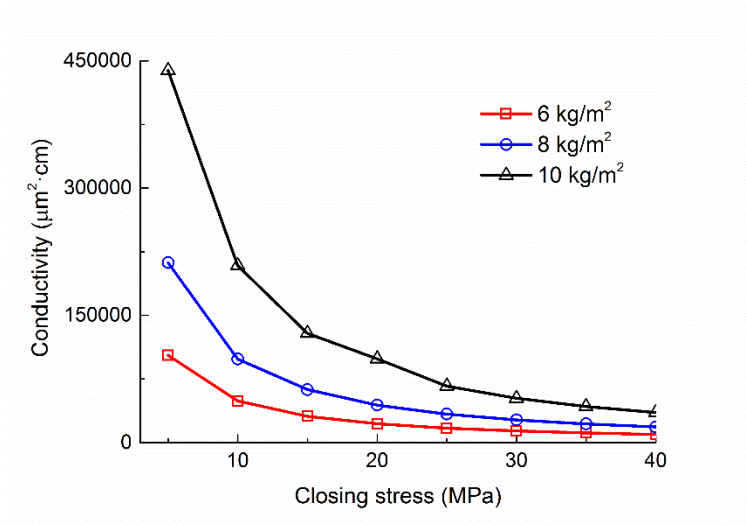


357

358 **Figure 12** Proppant pillar porosity and fracture aperture at different closing stress for three proppant  
 359 concentrations,  $6 \text{ kg/m}^3$ ,  $8 \text{ kg/m}^3$ , and  $10 \text{ kg/m}^3$

360

361 Figure 13 shows that the fracture conductivity for these three cases decreases quickly at  
 362 the early stage of the loading, due to the fact that both fracture aperture and proppant pillar  
 363 porosity experience a rapid decrease. When the closing stress rises from 5 MPa to 10 MPa,  
 364 the fracture conductivity with the proppant concentration of  $6 \text{ kg/m}^3$ ,  $8 \text{ kg/m}^3$ , and  $10 \text{ kg/m}^3$   
 365 decreases by 52.3%, 53.5%, and 52.4%, respectively. After the closing stress exceeds 30 MPa,  
 366 the fracture conductivity levels off, despite that the proppant pillar porosity changes from  
 367 decreasing to increasing. It can be concluded that the aperture change contributes more to the  
 368 fracture conductivity than the proppant porosity change.



369

370 **Figure 13** Fracture conductivity at different closing stress for three proppant concentrations, 6 kg/m<sup>3</sup>, 8

371

kg/m<sup>3</sup>, and 10 kg/m<sup>3</sup>

372

373 **4.3 Effect of time ratio  $\tau$** 

374

375

376

377

378

379

380

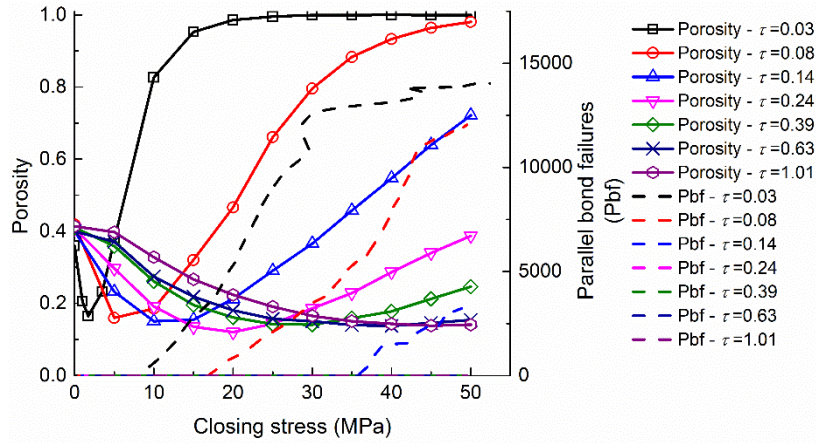
381

382

383

384

To investigate the effect of time ratio  $\tau$  on the fracture conductivity, a series of tests with  $\tau$  ranging from 0.03 to 1.01 are carried out. The initial proppant pillar height is assumed to be 6 mm, the proppant pillar radius varies for different  $\tau$ . The proppant concentration is 8 kg/m<sup>3</sup> for all cases. Figure 14 plots the proppant pillar porosity and cumulative parallel bond failures versus closing stress for different  $\tau$ . With the increase of closing pressure, the porosity of proppant pillar decreases first and then increases. The bigger the  $\tau$ , the less of the porosity change reversing. The number of parallel bond failures also decreases dramatically with the increase of  $\tau$ . As expected, the plot of fracture aperture versus closing stress for different time ratio  $\tau$  (Figure 15) shows that larger  $\tau$  leads to less closing of fracture aperture. The fracture aperture converges to the value for conventional fracturing when uniform layer of proppant is applied.



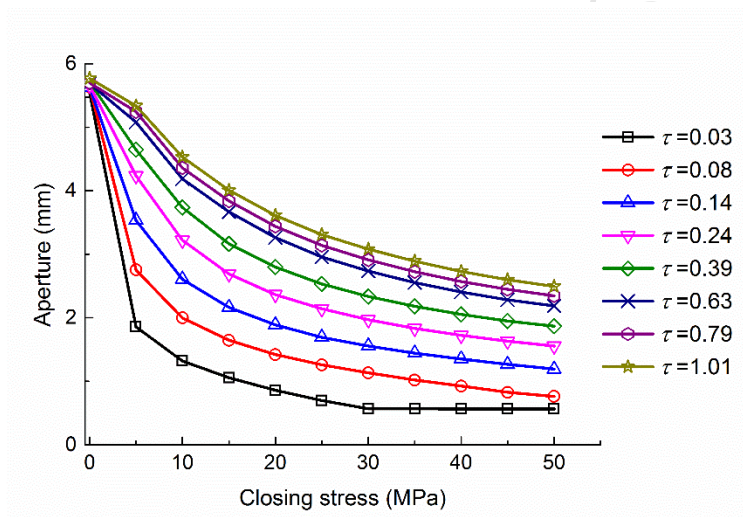
385

386

**Figure 14** Proppant pillar porosity and cumulative parallel bond failures versus closing stress for different time ratio  $\tau$

387

388



389

390

**Figure 15** Fracture aperture versus closing stress for different time ratio  $\tau$

391

392 Figure 16 shows the fracture conductivity versus time ratio  $\tau$  for different closing stress.

393 The fracture conductivity in general increases with the decrease of fracture closing stress. For

394 the given closing stress, the fracture conductivity increases first with the time ratio  $\tau$  and turns

395 to decrease later on as  $\tau$  further increases. The reason is that although larger  $\tau$  can lead to

396 larger aperture as shown in Figure 15, the decrease of fluid channel width could damage more

397 of the overall fracture conductivity. The peak of fracture conductivity lies at about  $\tau = 0.75$ .

398 The results suggest that the optimized range of  $\tau$  is about [0.5, 1.2].

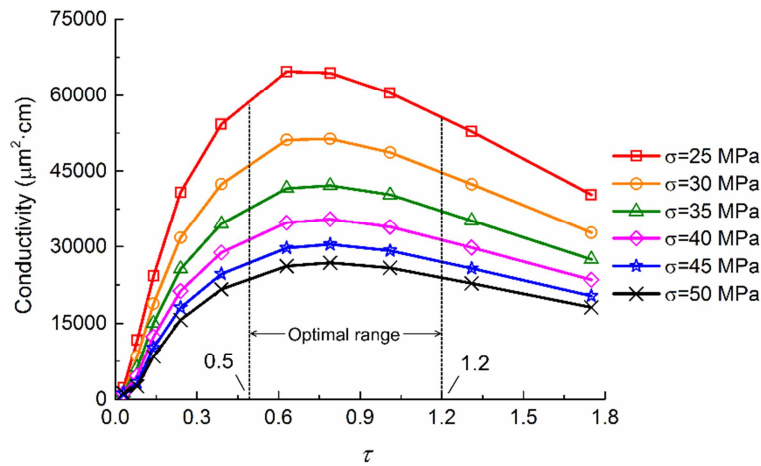


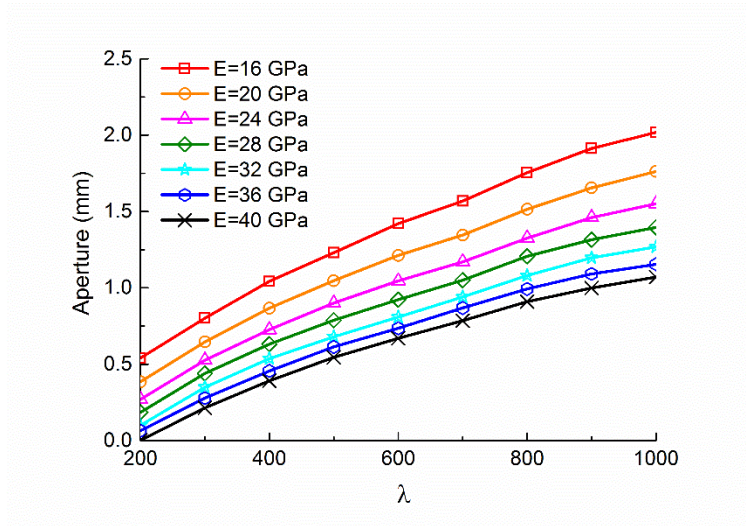
Figure 16 Fracture conductivity versus time ratio  $\tau$  for different closing stress

#### 4.4 Effect of elastic modulus to closing stress ratio

The ratio of elastic modulus of reservoir rock to closing stress is used as an index to evaluate the feasibility of channel fracturing,

$$\lambda = \frac{E}{\sigma} \quad (13)$$

The effect of elastic modulus to closing stress ratio  $\lambda$  on the fracture conductivity is studied by varying the elastic modulus of the reservoir rock and the fracture closing pressure. Figure 17 plots the fracture aperture versus ratio  $\lambda$  for different reservoir rock elastic modulus. The fracture closing stress is 41.4 MPa. The proppant size is 20/40 mesh and the proppant concentration is 8 kg/m<sup>3</sup>. For the same  $\lambda$  value, the larger the reservoir rock elastic modulus, the larger the closed pressure, the smaller the fracture aperture. The plot of fracture conductivity versus ratio  $\lambda$  for different rock elastic modulus (Figure 18) shows that the fracture conductivity increases as  $\lambda$  increases, and the fracture conductivity change is more sensitive to smaller elastic modulus.

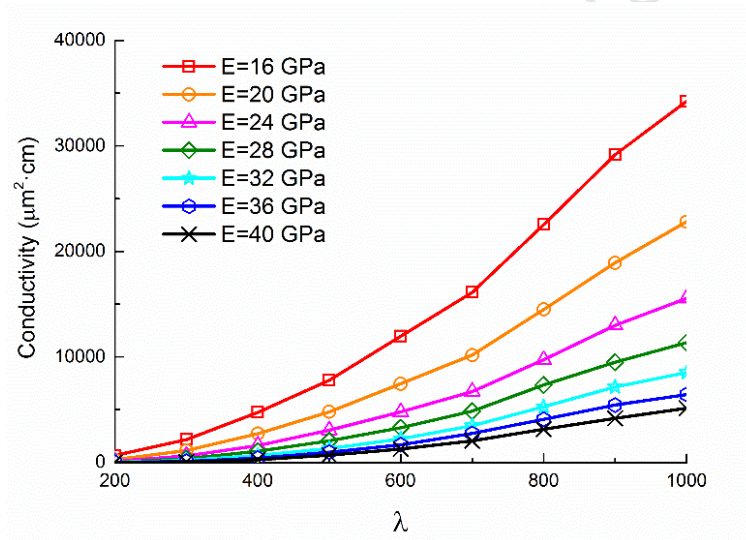


415

416

**Figure 17** Fracture aperture versus ratio  $\lambda$  for different reservoir rock elastic modulus

417



418

419

**Figure 18** Fracture conductivity versus ratio  $\lambda$  for different reservoir rock elastic modulus

420

421

422

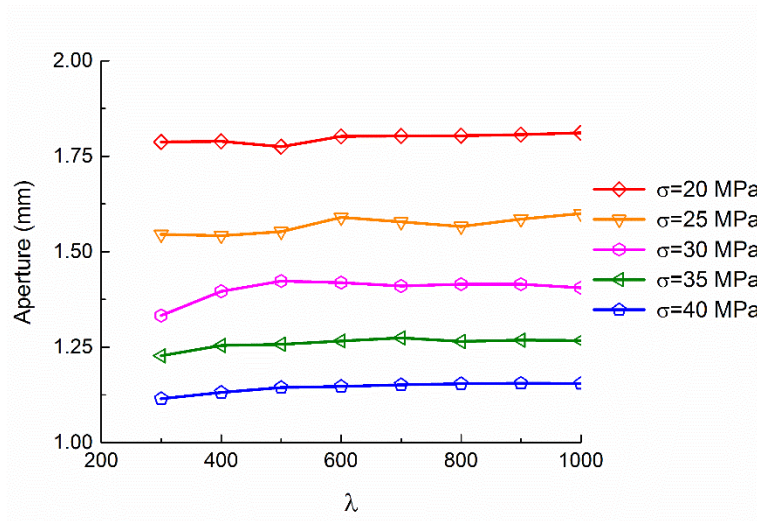
423

424

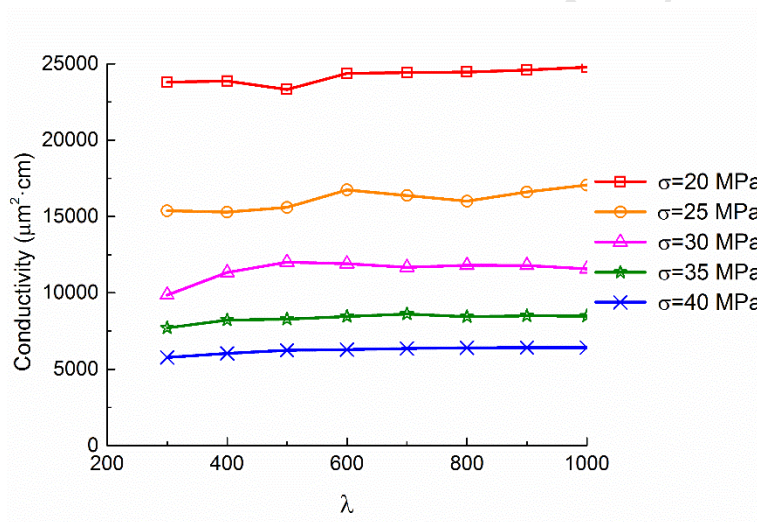
425

426

Figure 19 and Figure 20 plot the fracture aperture and fracture conductivity, respectively, at different ratio  $\lambda$  and different closing stress. According to the Eq. (13), with the same closing stress, the increase of  $\lambda$  means the increase of the elastic modulus of the rock. Both fracture aperture and fracture conductivity increase slightly with the increase of elastic modulus. It indicates that stiffer reservoir rock leads to larger fracture aperture after closing. This observation is consistent with the study of Deng et al. (2014).



427  
428  
429 **Figure 19** Fracture aperture versus ratio  $\lambda$  for different closing stress



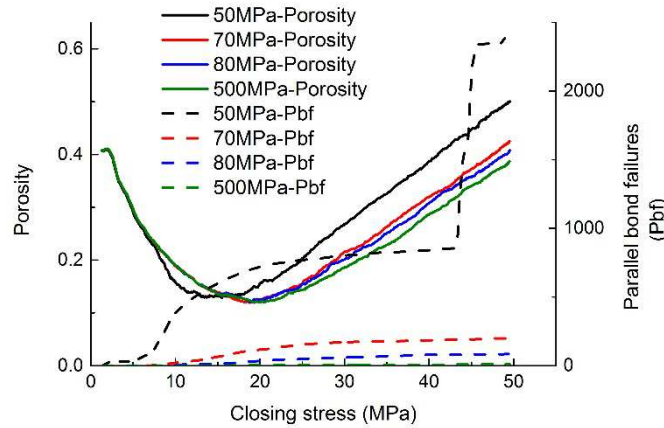
430  
431  
432 **Figure 20** Fracture conductivity versus ratio  $\lambda$  for different closing stress

## 433 5 Discussions

### 434 5.1 Evolution of proppant pillar porosity

435 The proppant pillar porosity during fracture closing generally decreases initially but  
436 tends to increase as the closing stress further increases. To investigate the evolution of  
437 proppant pillar porosity during fracture closing, parametric study of proppant particle bonding  
438 strength is carried out, which can be viewed as effectively varying the fiber strength. Figure  
439 21 plots the proppant pillar porosity and cumulative parallel bond failures at different closing  
440 stress for four bonding strength, 50 MPa, 70 MPa, 80 MPa and 500 MPa. The proppant  
441 concentration is  $8 \text{ kg/m}^3$ . The bond between two neighboring proppants will sustain the

442 applied force until the force exceeds the bond strength, which may lead to bond failure and  
 443 form microcracks. The results in Figure 21 reveals the link between the proppant pillar  
 444 stability, indicating by the number of bond failures, with the porosity increasing at the later  
 445 stage of the loading.

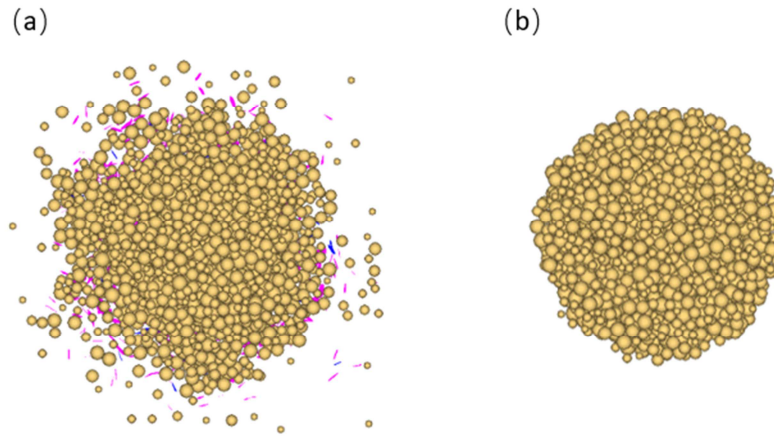


446

447 **Figure 21** Proppant pillar porosity and cumulative parallel bond failures at different closing stress for  
 448 four bonding strength, 50 MPa, 70 MPa, 80 MPa and 500 MPa

449

450 Figure 22 shows the profile of proppant pillar for the bond strength of 50 MPa and 500  
 451 MPa with bond failures displayed in pink and blue. Though whether parallel bond fails in  
 452 tension or in shear does not directly correlate with a tensile or shear failure mechanism at the  
 453 macro-scale, the parallel bond failures show micro-scale failure mechanism for pillars (Ma  
 454 and Huang 2018b). A large number of bond failures occur between the proppant particles  
 455 when the bond strength is small. And particles move outward and spread in a larger crossing  
 456 section area. This can explain the decreasing to increasing transition of porosity as the closing  
 457 stress is large enough to lead to the breakdown of the proppant pillar. The same explanation  
 458 can be applied to the effect of  $\tau$  on the porosity change as shown in Figure 14. Larger  $\tau$  leads  
 459 to larger diameter of the proppant pillar, thus the pillar becomes more stable and can maintain  
 460 the integrity at the end of the loading. As a result, the cases with larger  $\tau$  do not have the  
 461 porosity increasing at the later stage of the loading.

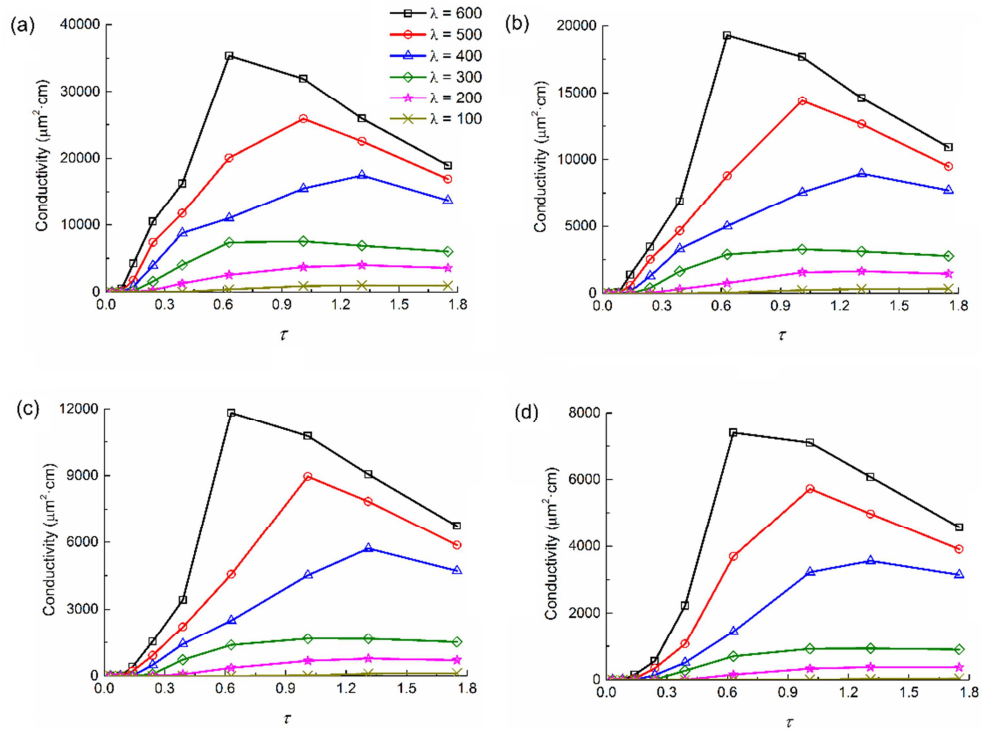


462  
 463 **Figure 22** Profile of proppant pillar under the fracture closing stress of 41.7 MPa, (a) 50 MPa bonding  
 464 strength, and (b) 500 MPa bonding strength; the pink and blue segments represent the tensile and shear  
 465 failures, respectively  
 466

## 467 5.2 Consideration of selecting $\tau$ in the field

468 The above analysis indicates that the time ratio  $\tau$  is the key parameter for fracturing  
 469 design for field application of channel fracturing. For given rock modulus, closing stress and  
 470 proppant size, the relationship between fracture conductivity and time ratio  $\tau$  can be  
 471 calculated by the proposed model in this study. Thus, the optimal range of  $\tau$  can be given as a  
 472 guidance for field operation. In field practice, however, the arrangement and shapes of  
 473 proppant pillars might not be as ideal as assumed in the model. Consequently, a slightly larger  
 474 value of  $\tau$  is recommended to better maintain the proppant pillar stability.

475 It was pointed out that if the ratio  $\lambda$  is less than 275, the reservoir is not suitable for  
 476 channel fracturing technology (Schlumberger 2012). In order to evaluate the reliability of this  
 477 criterion, we calculate relationship between conductivity and time ratio  $\tau$  for different  $\lambda$ , as  
 478 shown in Figure 23. The results show that for small elastic modulus of rock (e.g.,  $E = 16$  GPa  
 479 in Figure 23(a)), the fracture conductivity is not negligible when  $\lambda = 100$  or 200 and channel  
 480 fracturing might still be feasible.



481

482 **Figure 23** Relationship between conductivity and time ratio  $\tau$  for different  $\lambda$  by varying the elastic  
 483 modulus of rock, (a) 16 GPa, (b) 24 GPa, (c) 32 GPa, (d) 40 GPa

484

### 485 5.3 Analysis of field application of channel fracturing

486 Channel fracturing was tested in the A11 block of Shengli Oilfield of China and  
 487 compared with the conventional fracturing technique. A total of three conventional fracturing  
 488 wells and four channel fracturing well were completed. The thickness of the reservoir layer in  
 489 the A11 block is 32.5-51.5 m. The reservoir pressure coefficient is 1.47-1.64  $\text{g}/\text{cm}^3$ , the  
 490 permeability is 12.3-23.2 mD, and the porosity is 2.80%-16.10%. The minimum principal  
 491 stress is 49-56 MPa, the elastic modulus is 34 MPa, and the Poisson's ratio is 0.28. In the  
 492 channel fracturing treatment, the pump injection rate was 5-6  $\text{m}^3/\text{min}$  and the total injection  
 493 time was 75 minutes. The single pulse pumping time with 30/50 mesh proppant is 2-2.3 min  
 494 and the pumping time without proppant is 1.8-2 min. The detailed parameters for the seven  
 495 wells are listed in Table 3.

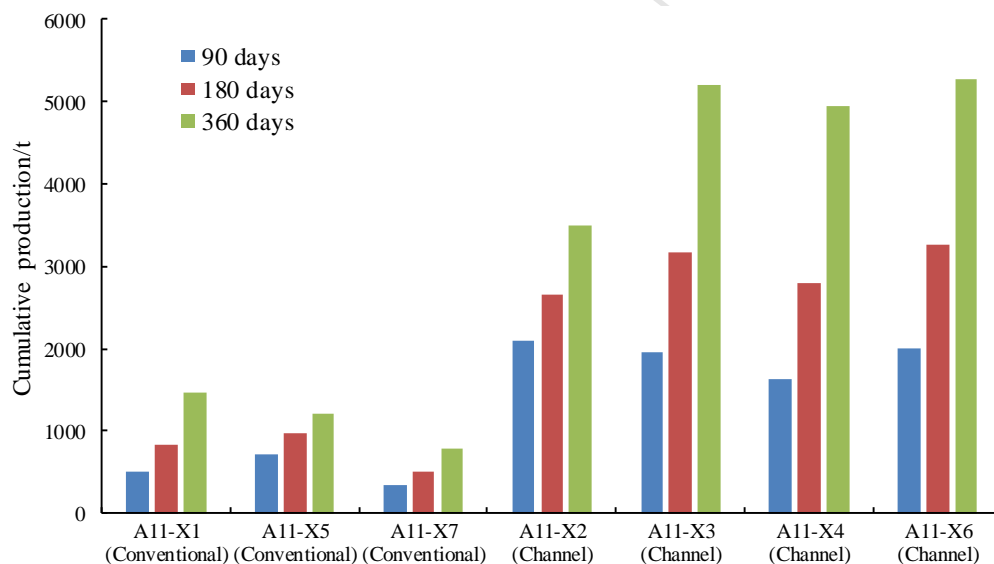
496

497

**Table 3** Parameters of three conventional fracturing wells and four channel fracturing well in the A11 block of Shengli Oilfield

Well id	Fracturing Type	Depth /m	Pay zone depth /m	Pressure Coefficient g/cm <sup>3</sup>	Minimum horizontal stress MPa	Permeability /10 <sup>-3</sup> μm <sup>2</sup>	Porosity	<i>t<sub>p</sub></i> /min	<i>t<sub>f</sub></i> /min	Proppant mass /m <sup>3</sup>	$\lambda$	$\tau$
A11-X1	Conventional	3578.0-3 670.0	30.2	1.48	50	23.2	10.20%			90	680	
A11-X5	Conventional	3636.8-3 766.0	36.6	1.47-1.64	51	6.7	10.20%			80	667	
A11-X7	Conventional	3676.5-3 719.1	30.3	1.47-1.64	51	12.3	10.20%			82	667	
A11-X2	Channel	3612.4-3 812.8	23.9	1.48	52	5.3	10.20%	2.04	1.82	52.7	654	1.12
A11-X3	Channel	3531.8-3 814.3	37.6	1.47-1.64	49	15.0	2.80%-16 .10%	2	1.8	36.6	694	1.11
A11-X4	Channel	3587.4-3 883.0	30.7	1.47-1.64	50	18.0	2.80%-16 .10%	2	1.8	52.8	680	1.11
A11-X6	Channel	3546.4-3 621.3	32.5	1.47-1.64	56	15.5	10.20%	2.23	2	41	607	1.12

498 Figure 24 compares the cumulative oil production of channel fracturing wells and  
 499 conventional fracturing wells in the A11 block. The channel fracturing wells generally exhibit  
 500 significantly higher production rate than conventional fracturing wells. The average 90-day  
 501 oil production, 180-day oil production, and 360-day oil production increase 262%, 274%, and  
 502 294%, respectively, compared with the conventional fracturing wells. At the same time, the  
 503 average growth rates of conventional fracturing wells from 90 days to 180 days and from 180  
 504 days to 360 days are 48.4% and 53.3%, respectively, while the average growth rates in  
 505 channel fracturing wells are 53.2% and 58%, which indicates that the fracture conductivity of  
 506 channel fracturing is more effective than conventional fracturing. For the A11-X2 well with  
 507 the lowest reservoir permeability, the channel fracturing has also achieved great success. The  
 508 360-day cumulative oil production is 2.5 times larger than that of the conventional fracturing  
 509 well A11-X5. The time ratio  $\tau$  of the channel fracturing in the A11 block is between 1.11 and  
 510 1.13, which falls into the optimized range recommended based on the proposed theoretical  
 511 model in this work.



512

513 **Figure 24** Comparison of cumulative oil production for three conventional fracturing wells and four  
 514 channel fracturing wells in the A11 block of Shengli Oilfield

515

## 516 6 Conclusions

517 In this study, an analytical model for channel fracturing conductivity is proposed by  
 518 regarding pillar and channel as two different flow media. The analytical solution is then  
 519 implemented in DEM modeling, which is capable of accounting for fracture closing and pillar  
 520 deformation. During the fracture closing process, the proppant pillar porosity first decreases  
 521 due to compression and then increases due to the breakdown of the proppant pillar and the

522 resulted particle movement outward, while the fracture conductivity generally decreases.

523 Channel fracturing conductivity increases with the increasing proppant size and proppant  
524 concentration. The ratio of the pulsing time of proppant laden fluid to the pulsing time of the  
525 clean fluid is the key parameter for the field operation. The numerical results show that a  
526 large value of time ratio  $\tau$  is able to enhance the pillar stability though it may lead to the  
527 damage of fracture conductivity. For given rock modulus, closing stress and proppant size, the  
528 optimal range of  $\tau$  can be given as a guidance for field operation. The field application of  
529 channel fracturing in the Shengli Oilfield proves that the optimized range of time ratio  $\tau$  based  
530 on the proposed theoretical model in this work is valid. This paper gives insights for  
531 understanding the channel fracture conductivity and provides a practical tool for the  
532 optimization of channel fracturing design in the field.

### 533 **Acknowledgements**

534 This work was funded by the National Key Basic Research Program of China (973  
535 Program, No. 2014CB239205), the National Natural Science Foundation of China (No.  
536 51604232, 41772286) and the China Postdoctoral Science Foundation (No. 2017M610117).  
537 The authors also sincerely thank Itasca for providing education loan of PFC3D software.

### 538 **Reference**

- 539 Asgian, M.I., Cundall, P.A., Brady, B.H.G., 1995. The mechanical stability of propped hydraulic  
540 fractures: a numerical study. *Journal of Petroleum Technology* 47(03): 203-208.
- 541 Bear, J., 1972. *Dynamics of fluids in porous media*. American Elsevier Publishing, New York.
- 542 Bolintineanu, D.S., Rao, R.R., Lechman, J.B., et al., 2017. Simulations of the effects of proppant  
543 placement on the conductivity and mechanical stability of hydraulic fractures. *International*  
544 *Journal of Rock Mechanics and Mining Sciences* 100:188-198.
- 545 Cundall, P.A., Strack, O.D.L., 1979. A discrete numerical model for granular assemblies. *Géotechnique*  
546 29(1):47-65.
- 547 Deng, S., Li, H., Ma, G., et al., 2014. Simulation of shale-proppant interaction in hydraulic fracturing  
548 by the discrete element method. *International Journal of Rock Mechanics & Mining Sciences*  
549 70:219-228.
- 550 Gawad, A.A., Long, J., El-Khalek, T., et al., 2013. Novel combination of channel fracturing with  
551 rod-shaped proppant increases production in the Egyptian Western Desert. In: *SPE European*  
552 *Formation Damage Conference and Exhibition*, Noordwijk, The Netherlands, 5-7 June.
- 553 Gazi, N.H., Al-Othman, M., Tirkey, N., et al., 2016. Channel-Fracturing Technique Successfully  
554 Unlock Oil Reserve in Shallow Low Temperature Sandstone Reservoir in the South East Kuwait.  
555 In: *Abu Dhabi International Petroleum Exhibition & Conference*.
- 556 Gillard, M., Medvedev, O., Peña, A., et al., 2010. A New Approach to Generating Fracture Conductivity.  
557 In: *SPE Annual Technical Conference and Exhibition*, Florence, Italy, 20-22 September.
- 558 Guo, J.C., Wang, J.D., Liu, Y.X., et al., 2017. Analytical analysis of fracture conductivity for sparse  
559 distribution of proppant packs. *Journal of Geophysics and Engineering* 2017(14):599-610.

- 560 Hou, B., Zheng, X.J., Chen, M., et al., 2016. Parameter simulation and optimization in channel  
561 fracturing. *Journal of Natural Gas Science and Engineering* 35:122-130.
- 562 Hou, T.F., Zhang, S.C., Yu, B.H., et al., 2016. Theoretical Analysis and Experimental Research of  
563 Channel Fracturing in Unconventional Reservoir. In: *SPE Europec featured at 78th EAGE*  
564 *Conference and Exhibition, Vienna, Austria, 30 May-2 July.*
- 565 Kayumov, R., Klyubin, A., Yudin, A., et al., 2012. First Channel Fracturing Applied in Mature Wells  
566 Increases Production from Talinskoe Oilfield in Western Siberia. In: *SPE Russian Oil & Gas*  
567 *Exploration & Production Technical Conference and Exhibition, Moscow, Russia, 16-18 October.*
- 568 Li, A.Q., Mu, L.J., Li, X.W., et al., 2015. The Channel Fracturing Technique Improves Tight Reservoir  
569 Potential in the Ordos Basin, China. In: *SPE/IATMI Asia Pacific Oil & Gas Conference and*  
570 *Exhibition, Nusa Dua, Bali, Indonesia, 20-22 October.*
- 571 Li, K., Gao, Y., Lyu, Y., et al., 2015. New mathematical models for calculating proppant embedment  
572 and fracture conductivity. *SPE Journal* 20(03):496-507.
- 573 Ma, Y., Huang, H., 2018a. A displacement-softening contact model for discrete element modeling of  
574 quasi-brittle materials. *International Journal of Rock Mechanics and Mining Sciences* 104:9-19.
- 575 Ma, Y., Huang, H., 2018b. DEM analysis of failure mechanisms in the intact Brazilian test.  
576 *International Journal of Rock Mechanics and Mining Sciences* 102: 109-119.
- 577 Medvedev, A.V., Kraemer, C.C., Pena, A.A., et al., 2013. On the Mechanisms of Channel Fracturing. In:  
578 *SPE Hydraulic Fracturing Technology Conference, 4-6 February, The Woodlands, Texas, USA.*
- 579 Meyer, B.R., Bazan, L.W., Walls, D.E., et al., 2014. Theoretical Foundation and Design Formulae for  
580 Channel and Pillar Type Propped Fractures – A Method to Increase Fracture Conductivity. In: *SPE*  
581 *Annual Technical Conference and Exhibition, Amsterdam, The Netherlands, 27-29 October.*
- 582 Nguyen, P.D., Vo, L.K., Parton, C., et al., 2014. Evaluation of Low-Quality Sand for Proppant-Free  
583 Channel Fracturing Method. In: *International Petroleum Technology Conference.*
- 584 Potyondy, D.O., Cundall, P.A., 2004. A bonded-particle model for rock. *International Journal of Rock*  
585 *Mechanics and Mining Sciences* 41(8): 1329-1364.
- 586 Rhein, T., Loayza, M., Kirkham, B., et al., 2011. Channel Fracturing in Horizontal Wellbores: the New  
587 Edge of Stimulation Techniques in the Eagle Ford Formation. In: *SPE Annual Technical*  
588 *Conference and Exhibition, Denver, USA, 30 October - 2 November.*
- 589 Samuelson, M., Stefanski, J., Downie, R., et al., 2012. Field Development Study: Channel Fracturing  
590 Achieves Both Operational and Productivity Goals in the Barnett Shale. In: *Americas*  
591 *Unconventional Resources Conference, Pittsburgh, Pennsylvania, USA, 5-7 June.*
- 592 Schlumberger, 2012. HiWAY: the Quest for Infinite Conductivity Innovation for a Step-change in  
593 Hydraulic Fracturing.
- 594 Valenzuela, A., Guzmán, J., Chávez, S., et al., 2012. Field Development Study: Channel Fracturing  
595 Increases Gas Production and Improves Polymer Recovery in Burgos Basin, Mexico North. In:  
596 *SPE Hydraulic Fracturing Technology Conference, The Woodlands, Texas, USA, 6-8 February.*
- 597 Valiullin, A., Vladimir, M., Yudin, A., et al., 2015. Channel Fracturing Technique Helps to Revitalize  
598 Brown Fields in Langepas Area. In: *SPE Oil and Gas India Conference and Exhibition, Mumbai,*  
599 *India 24-26 November.*
- 600 Yan, X., Huang, Z.Q., Yao, J., et al., 2016. Theoretical analysis of fracture conductivity created by the  
601 channel fracturing technique. *Journal of Natural Gas Science and Engineering* 31:320-330.
- 602 Zhang, F. Dontsov, E., Mack. M., 2017. Fully coupled simulation of a hydraulic fracture interacting  
603 with natural fractures with a hybrid discrete-continuum method. *International Journal Numerical*

- 604 Analytical Methods in Geomechanics 41:1430–1452.
- 605 Zhang, F.S., Zhu, H.Y., Zhou, H.G., et al., 2017. Discrete-Element-Method/  
606 Computational-Fluid-Dynamics Coupling Simulation of Proppant Embedment and Fracture  
607 Conductivity After Hydraulic Fracturing. SPE Journal 22(2):632-644.
- 608 Zhang, J.C., 2014. Theoretical conductivity analysis of surface modification agent treated proppant.  
609 Fuel 134:166-170.
- 610 Zhang, J.C., Hou, J.R., 2016. Theoretical conductivity analysis of surface modification agent treated  
611 proppant II – Channel fracturing application. Fuel 165:28-32.
- 612 Zheng, X.J., Chen, M., Hou, B., et al., 2017. Effect of proppant distribution pattern on fracture  
613 conductivity and permeability in channel fracturing. Journal of Petroleum Science and  
614 Engineering 149:98-106.
- 615 Zhou, J., Huang, H., Deo M., 2015. Modeling the interaction between Hydraulic and Natural Fractures  
616 using Dual-Lattice Discrete Element Method, The 49th US Rock Mechanics/Geomechanics  
617 Symposium, San Francisco, California, June 28-July 1. ARMA 15-507.
- 618 Zhou, J., Huang, H., Deo M., Jiang, S., 2015. A New Physics-Based Modeling of Multiple NonPlanar  
619 Hydraulic Fractures Propagation, Unconventional Resources Technology Conference, San  
620 Antonio, Texas, July 20-22. URTeC-2170875-MS.
- 621 Zhu, H.Y., Shen J.D., Zhang F.S., et al., 2018. DEM-CFD Modeling of Proppant Pillar Deformation  
622 and Stability during the Fracturing Fluid Flowback. Geofluids, 2018: 3535817.

- During the fracture closing process, the proppant pillar porosity first decreases due to compression and then increases because of the breakdown of the proppant pillar and the resulted particle movement outward, while the fracture conductivity generally decreases.
- The ratio of the pulsing time of proppant laden fluid to the pulsing time of the clean fluid is the key parameter for the field operation.
- For given rock modulus, closing stress and proppant size, the optimal range of time ratio exists as a guidance for field operation.